A&A 631, A120 (2019)
https://doi.org/10.1051/0004-6361/201935491

Astronomy & Astrophysics

Quasars as standard candles II

The non-linear relation between UV and X-ray emission at high redshifts

F. Salvestrini[1,2], G. Risaliti[3,4], S. Bisogni[3,4], E. Lusso[3,4,5], and C. Vignali[1,2]

[1] Dipartimento di Astronomia, Università degli Studi di Bologna, via Gobetti 93/2, 40129 Bologna, Italy
e-mail: francesc.salvestrin2@unibo.it
[2] INAF – Osservatorio di Astrofisica e Scienza dello Spazio di Bologna, via Gobetti 93/3, 40129 Bologna, Italy
[3] Dipartimento di Fisica e Astronomia, Università di Firenze, Via G. Sansone 1, 50019 Sesto Fiorentino, FI, Italy
[4] INAF, Osservatorio Astrofisico di Arcetri, Largo E. Fermi 5, 50125 Firenze, Italy
[5] Centre for Extragalactic Astronomy, Durham University, South Road, Durham DH1 3LE, UK

Received 18 March 2019 / Accepted 18 September 2019

ABSTRACT

A tight non-linear relation between the X-ray and the optical-ultraviolet (UV) emission has been observed in active galactic nuclei (AGN) over a wide range of redshift and several orders of magnitude in luminosity, suggesting the existence of an ubiquitous physical mechanism regulating the energy transfer between the accretion disc and the X-ray emitting corona. Recently, our group developed a method to use this relation in observational cosmology, turning quasars into standardizable candles. This work mainly seeks to investigate the potential evolution of this correction at high redshifts. We thus studied the $L_X - L_{UV}$ relation for a sample of quasars in the redshift range $4 < z < 7$, adopting the selection criteria proposed in our previous work regarding their spectral properties. The resulting sample consists of 53 type 1 (unobscured) quasars, observed either with *Chandra* or *XMM-Newton*, for which we performed a full spectral analysis, determining the rest-frame 2 keV flux density, as well as more general X-ray properties such as the estimate of photon index, and the soft (0.5–2 keV) and hard (2–10 keV) unabsorbed luminosities. We find that the relation shows no evidence for evolution with redshift. The intrinsic dispersion of the L_X–L_{UV} for a sample free of systematics/contaminants is of the order of 0.22 dex, which is consistent with previous estimates from our group on quasars at lower redshift.

Key words. quasars: general – galaxies: high-redshift – galaxies: active – X-rays: galaxies

1. Introduction

An observational non-linear relation between the UV and X-ray monochromatic luminosities in active galactic nuclei (AGN) has been known for decades ($L_X \propto L_{UV}^{\gamma}$; e.g. Avni & Tananbaum 1986). This relation shows a slope γ around 0.6 over several orders of magnitude in luminosity and up to high redshifts irrespective of the sample selection (e.g. X-ray or optically selected samples; Vignali et al. 2003a; Strateva et al. 2005; Steffen et al. 2006; Just et al. 2007; Lusso et al. 2010; Young et al. 2010), suggesting that a universal physical mechanism drives the non-linear dependence between the X-ray and UV emission. These properties indicate that the physical mechanism responsible for the observed relation has to be universal. Indeed, these sources are powered by the accretion of matter onto the central supermassive black hole (SMBH), through an accretion disc (Shakura & Sunyaev 1973), where the gravitational energy of the in-falling material is efficiently transformed into UV radiation. This is the so-called big blue bump (BBB), which is the major contribution to the spectral energy distribution (SED) of a quasar. The observed emission in the X-ray band (corresponding to ∼1−10% of the total power; e.g. Lusso et al. 2012) is due to inverse-Compton reprocessing of seed photons from the disc, by a corona of hot electrons located in the vicinity of the SMBH (e.g. Haardt & Maraschi 1993). To maintain stable emission, the hot coronal gas needs to be continuously reheated, but the physical process responsible for the steady energy transfer from the disc to the corona is not yet well understood. A fully consistent physical model able to predict the observed relation has yet to be found even though some toy models have been proposed (e.g. Haardt & Maraschi 1991, 1993; Svensson & Zdziarski 1994; Di Matteo 1998; Merloni 2003; Lusso & Risaliti 2017). A better understanding of the properties of the L_X–L_{UV} relation can provide stringent constraints on the unknown physical process which stands behind it. Recently, our group developed a technique that uses this non-linear relation in observational cosmology, turning quasars into standardizable candles (Risaliti & Lusso 2015). This technique allows us to study the evolution of the universe in the redshift range $2 < z < 7.5$, which has been poorly investigated by other cosmological probes such as type Ia supernovae ($z < 1.4$; Betoule et al. 2014) and baryon acoustic oscillations (BAO at $z \sim 2$; Aubourg et al. 2015; du Mas des Bourboux et al. 2017); one exception to this is gamma-ray bursts (e.g. Ghirlanda et al. 2004). Since a potential evolution of the relation with redshift could hamper the use of quasars as cosmological tools, in this work we investigate the presence of potential systematics of the L_X–L_{UV} relation at high redshifts, using the largest quasar sample available in the redshift range $4 < z < 7$ of finely selected objects, and taking advantages of the method developed by our group in previous works. The paper is organised as follows: In Sect. 2 we introduce the sample and the selection criteria adopted; in Sect. 3 and in Sect. 4 we outline the procedures performed to obtain the X-ray and UV flux estimates,

respectively; in Sect. 5 the analysis of the relation is presented, along with the results, and in Sect. 6 the conclusions of this work are presented. The luminosity distances were estimated assuming a concordance flat ΛCDM model with the matter density parameter $\Omega_M = 0.30$, the dark energy density parameter $\Omega_\Lambda = 0.70$, and the Hubble constant $H_0 = 70\,\mathrm{km\,s^{-1}\,Mpc^{-1}}$ (Komatsu et al. 2009).

2. Sample selection

In the last few years, our group proved that the L_X−L_{UV} relation in quasars is actually tight (∼0.2 dex) once accurate selection criteria are applied and systematic effects are properly taken into account (e.g. non-simultaneity or variability of the observations, gas absorption, dust reddening, and host galaxy contamination). In this paper, we selected a sample of high-redshift quasars spectrally classified as type 1 (i.e. unobscured), and possibly observed with the same facility, to maintain the sample as homogeneous as possible and to avoid potential systematic effects, which could lead to a larger observed dispersion.

As discussed before, we are interested in the study of the relation at the highest redshift; therefore we considered the updated catalogue by Brandt et al. (2004)[1], which consists of 158 quasars with redshift in the interval $3.96 < z < 7.08$, detected in the X-rays. We selected the 138 optically selected quasars out of the original 158, which have been observed either with *Chandra* or *XMM-Newton*. We then included SDSS J114816.7+525150.4 at $z = 6.43$ and SDSS J010013.0+280225.9 at $z = 6.30$, which were both observed with *XMM-Newton*, from the catalogue of high-redshift quasars by Nanni et al. (2017). Given the 140 sources with at least one X-ray observation, we searched for the UV coverage following this approach: (i) We cross matched our sample with the catalogue by Shen et al. (2011), which provides the rest-frame 2500 Å flux density for 36 out of the 138 quasars in the redshift range $4.01 < z < 4.99$. (ii) We then cross matched the remaining 104 objects with the *Sloan Digital Sky Survey* (SDSS) Data Release 7 (DR7; Abazajian et al. 2009) and Data Release 12 (DR12; Pâris et al. 2017) catalogues, providing the optical/UV spectra for 6 and 4 additional quasars, respectively, in the redshift range $5.0 < z < 5.4$. (iii) For sources with a redshift $z > 5.4$, we searched in the literature for their UV spectra and we found data for 12 of these, which have been observed with a number of different facilities from the SDSS; the references for each source are provided at the bottom of Table A.1. Further discussion on the adopted rest-frame 2500 Å monochromatic flux estimates for each group of sources is provided in Sect. 4.

The resulting sample consists of 58 quasars in the redshift range $4.01 < z < 7.08$, which benefit from a moderate-quality coverage in UV and X-ray bands.

We then applied to this sample a series of selection criteria following the procedure presented by Lusso & Risaliti (2016). Specifically, we chose unobscured optically selected quasars, classified as radio quiet sources (i.e. with radio-loudness parameter $R = F_{\nu,6\,\mathrm{cm}} / F_{\nu,4400\,\text{Å}}$ lower than 10, in this work 57/58), showing no broad absorption line features (identified as BAL in the literature, 4 in the sample).

Our final clean sample of high redshift objects is thus composed of 53 objects spanning the redshift range $4.01 < z < 7.08$. Taking advantage of the spectral and spatial resolution of the X-ray observations from *Chandra* and *XMM-Newton*, we performed a full spectral analysis on the archival data of the quasars in the sample. We catalogued the X-ray properties (i.e. spectral index, rest-frame 2 keV monochromatic flux, rest-frame 0.5–2 keV, and 2–10 keV X-ray luminosities) for the sample in Table A.1. The distribution of the 53 sources in terms of soft X-ray luminosity and redshift is presented in Fig. 1.

[1] http://personal.psu.edu/wnb3/papers/highz-xray-detected.txt

3. X-ray data

3.1. X-ray data reduction

Of the 53 quasars, 47 objects were observed with *Chandra* and 9 with *XMM-Newton* (ULAS J1120+0641, SDSS J114816.7+525150.4, and SDSS 1030+0524 were observed with both). For each observation, we followed the standard data reduction procedures for each telescope, obtaining a background-subtracted spectrum in the ∼0.1–10 keV band. We reprocessed *Chandra* data using the dedicated software CIAO v. 4.9. For on-axis observations (i.e. with source off-axis angle $\theta < 1'$), we extracted the source and background counts from a circular radius of 2″, centred on the source optical position, corresponding to 95% of the encircled energy fraction (EEF) at 1.5 keV. Counts from off-axis sources ($\theta > 1'$) were selected using 10″ radius circular regions, corresponding to at least 90% of the EEF. Background counts were extracted from contiguous source-free circular regions with ∼15″ radii.

In the case of XMM EPIC data we performed a step-by-step procedure using the Science Analysis Software (SAS) v16. For each observation, we filtered for time intervals of high background. We merged the two EPIC-MOS observations to increase the signal-to-noise ratio, while the EPIC-pn observation was reduced independently.

Source and background counts were extracted from a circular region centred at the optical position of quasi-stellar objects with radius of 15″ for on-axis positions, corresponding to 70% of the EEF ad 1.5 keV, 30″ for off-axis observations, equivalent to at least 40% of EEF at 1.5 keV. Background counts were extracted from contiguous source-free circular regions with ∼60″ radii.

3.2. X-ray analysis

For the X-ray spectral analysis we used the software XSPEC v. 12.9 (X-Ray Spectral Fitting Package; Arnaud et al. 1996). We assumed a *cstat* statistic (Poisson data) for the majority of the spectra, and a χ^2 statistic (Gaussian data) in the case of *XMM-Newton* observations having a number of counts >100. Galactic absorption is included in all the spectral models and the fluxes presented in Table A.1 are corrected for this effect.

The sample is a collection of unobscured (type I) quasars; their spectra are typically dominated by continuum emission. Additional features have been observed in the X-ray spectra of type I AGN: fluorescence emission lines from the neutral iron (e.g. Fe Kα and Kβ lines at rest-frame 6.40 and 7.06 keV, respectively), emission lines from the ionised iron (e.g. Fe XXV and XXVI at rest-frame 6.70 and 6.97 keV, respectively), and a potential reflection component by the torus or the accretion disc. The inclusion of model components either for the potential emission lines or reflection hump, which has been found to be weak in luminous type I quasars at high redshift (e.g. Shemmer et al. 2005), was not possible in the vast majority of the observations collected in this work owing to the relatively low photon counts statistics of the spectra. In the few observations with a relatively higher statistics, we tried to include additional Gaussian components among those discussed above, but

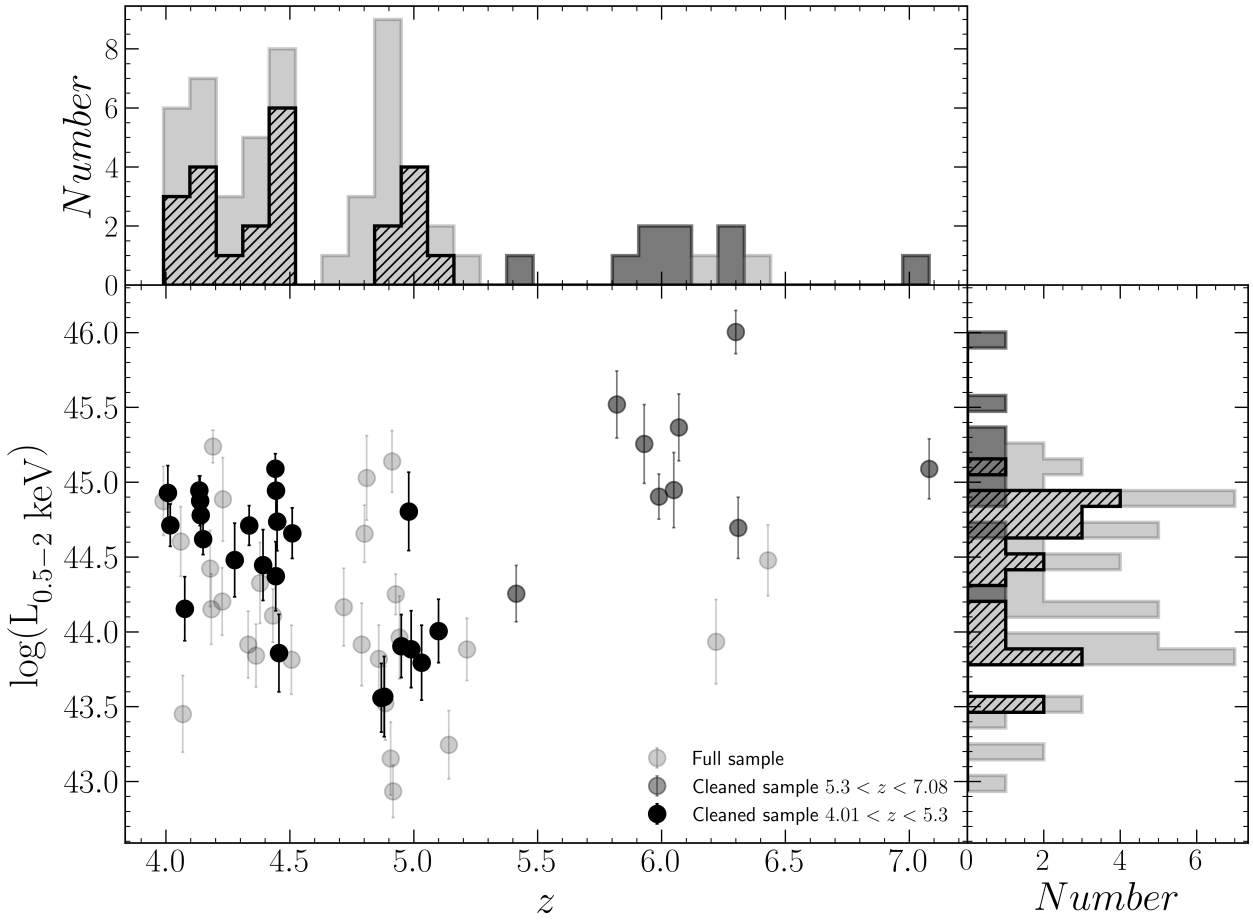

Fig. 1. *Central panel*: distribution of the estimated rest-frame soft X-ray luminosity (0.5–2 keV) vs. redshift for the final sample. The cleaned sample of 22 sources with $z < 5.3$ are indicated in solid black; in dark grey we report those selected at $z > 5.3$ (9 out of 53); the remaining (22/53) in light grey indicate those not included in the analysis because of the selection criteria applied (e.g. X-ray flux upper limits or too steep or flat X-ray spectral slope). *Top panel and right panel*: redshift and soft X-ray luminosity distribution of the final quasar sample, respectively. The colour coding adopted is the same used in the central panel except for the hatched black filling instead of solid.

they did not significantly improve the quality of the fit and the parameters were not constrained (considering the 90 per cent confidence level). Therefore, the adopted model consists of a single power law for the primary emission, where the slope and normalisation are free parameters. When the number of counts was not sufficient to perform a full spectral analysis, we evaluated an upper limit to flux density, freezing the power-law slope at $\Gamma = 1.9$, which is the average value for unobscured quasars (e.g. Vignali et al. 2003b, Nanni et al. 2017). This occurred for nine sources, properly flagged in Table A.1. For *XMM-Newton* observations we fitted together the EPIC-pn and the merged EPIC-MOS spectra, introducing a cross-calibration constant between the two datasets to account for the different camera responses. The values obtained for this constant are fully consistent within 8% (e.g. Read et al. 2014). In the case of multiple observations from the same telescope, we adopted the following approach: First, we chose the observation with the longest exposure if the difference between two observations was significant; for instance in the case of PSS0133+0400 we chose the 64 ks observation instead of the 6 ks observation. Second, we checked for any potential variability both in the slope and in the flux and, if the results from the fitting procedures were consistent within the uncertainties, we jointly fitted all the observations with the same model, with a free cross-normalisation constant for any potential minor variability in the flux or calibration within different observations. If the sources were observed with *Chandra* and *XMM-Newton*, we compared the two best-fit models to test for X-ray variability. We then considered the result from the model with the longest exposure time or, in case of similar exposure times, we used the best-fit parameters from the model with the lowest χ^2.

We estimated the fluxes by integrating the continuum emission over a given energy band (e.g. rest-frame 0.5–2 keV). To this purpose, we used the *cflux* convolution model in XSPEC, which provides the integrated emission and the associated uncertainty. Given the redshift of the sample ($4 < z < 7$), the soft band (rest-frame 0.5–2 keV) was marginally detected by *Chandra* and *XMM-Newton* only for the sources with the lowest redshift ($z < 5.5$). Then, the soft band fluxes (and luminosities) were estimated from the extrapolation of the power law fitted to the hard band (rest-frame 2–10 keV) spectrum, assuming that this emission follows the same law. We estimated the rest-frame 2 keV flux density by dividing the flux of the continuum emission over a narrow energy band (corresponding to rest-frame 0.01 keV) centred on the rest-frame 2 keV by the width of the energy band itself. In the case of sources with a redshift for which the rest-frame 2 keV fell outside the observable energy bands of *Chandra* and *XMM-Newton*, we estimated the fluxes from the extrapolation of the power law by modelling the continuum emission in the rest-frame hard band.

Apart from one case that we briefly discuss below, we did not find evidence for significant X-ray variability. This is in agreement with the results from recent works on the monitoring of samples of high-redshift quasars, which showed that these objects appear to be less variable in the X-rays with respect to AGN in the local Universe (e.g. Shemmer et al. 2017). The only source showing evidence for a strong X-ray variability is SDSS 1030+0524, which has been the target of three different observations over 15 years. The recent 500 ks monitoring by *Chandra*, presented by Nanni et al. (2018), confirmed the source properties obtained from the previous 2002 observation with the same telescope, but are in significant disagreement with those from the 2003 *XMM-Netwon* observation. The observed variability, affecting both the flux (up to a factor ∼2.5) and the spectral shape, raises questions about the potential variability in quasars observed when the Universe had less than 1 Gyr, when these sources could still be going through the early stages of their evolution. In this particular case, the low monitoring and poor counting statistics do not allow us to disentangle different scenarios; for example the variation in the obscuration level along the line of sight (as observed in local AGN, e.g. Risaliti et al. 2007) or variation in the accretion process onto the central SMBH. Further investigations on this issue are needed, but they require long-term monitoring and higher statistics observations for these high-redshift sources. Except for this particular case, there are no hints of any significant evolution in the X-ray properties of our properly selected samples of quasars.

In Table A.1 we present the X-ray properties of our sample, i.e. the spectral slope and estimates of the fluxes. We found results which are in agreement, within the uncertainties, with literature works on similar collection of high-redshift quasars (e.g. Nanni et al. 2017; Shemmer et al. 2017). We observe a mean spectral slope $\Gamma = 1.9$ with a dispersion of ∼0.5, in agreement with the spectral properties of quasars at similar and lower redshifts ($1 < z < 5.5$; e.g. Shemmer et al. 2006; Just et al. 2007; Vignali et al. 2005).

4. Optical data

The proxy of the UV luminosity is usually obtained from the rest-frame 2500 Å flux density. For a large part of the sources in our sample (33 out of 53), which were included in the SDSS DR7, we adopted the values compiled by Shen et al. (2011). The authors provided the 2500 Å flux density only for the sources that have a redshift $z \lesssim 5$, since there are no spectral windows free of emission lines at higher redshift, where they can accurately fit the continuum within the SDSS wavelength coverage (3800–9200 Å). In particular, the authors performed a spectral fit on the available spectral windows (i.e. up to the observed frame 9200 Å) with a power law for the continuum emission and a template including FeII and many emission lines (see Shen et al. 2011 for further details). Then, they extrapolated the rest-frame 2500 Å flux density using the slope of the continuum obtained from the fit.

For the remaining sources in our sample observed within the SDSS DR7 (6/53), for which Shen et al. (2011) do not provide a 2500 Å flux density measurement (i.e. $z > 5$), or observed within the SDSS DR12 (4/53), we obtained the monochromatic UV flux assuming the continuum spectrum to be a power law $S \propto \nu^{-\alpha}$ with $\alpha = 0.50$ (e.g. Vanden Berk et al. 2001; Lusso et al. 2015). We then used this slope to extrapolate the value at 2500 Å; we started from the median flux value in the rest-frame 1430–1470 Å waveband, which is the last (shortest wavelength) continuum window free from emission lines and for which the intergalactic medium absorption is not relevant (Lusso et al. 2015). The reliability of this method (i.e. the extrapolation of the flux density with a fixed slope) is discussed in Appendix B.

In the case of quasar at redshift higher than 5.5, the SDSS wavelength coverage is probing the far UV (i.e. $\lambda < 1450$ Å at

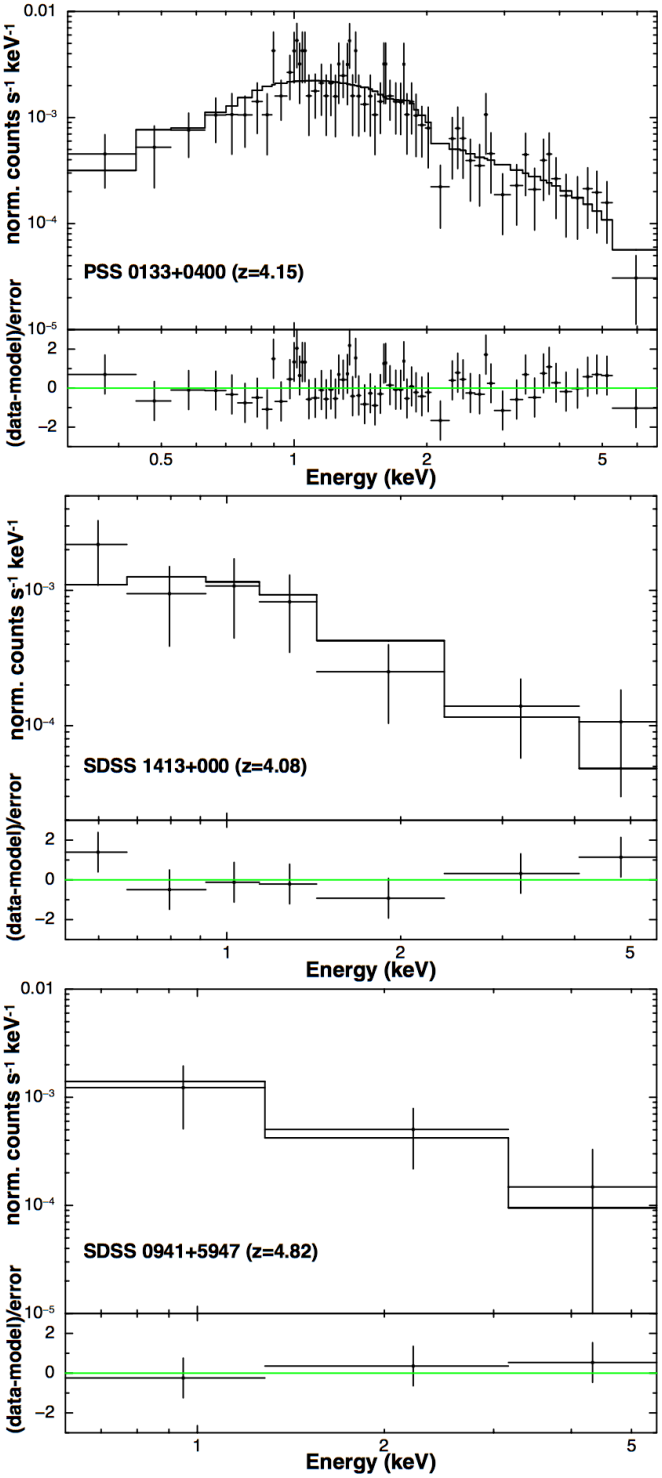

Fig. 2. Examples of spectra of three quasars with decreasing statistics, *from top to bottom*. The best-fit models (consisting of a power law modified by galactic absorption) and the data are plotted in each of the *top panels*, as functions of the observed-frame energies in units of keV. The residuals (data minus model, in units of sigma) are shown in the *bottom panels*.

the rest frame), so we searched in the literature for any optical or NIR observations from which we could estimate the rest-frame 2500 Å flux density (10 sources out of 53 have $z > 5.5$). Given the number of different telescopes used to observe this set of sources (references in Table A.1), the UV flux estimates can be affected by a larger dispersion due to potential cross-calibration uncertainties among different cameras. To assess the potential contribution of this effect on the shape of the L_X–L_{UV} relation, in Sect. 5 we presented the results obtained with and without the inclusion of this high-redshift subsample.

Since the catalogue published by Shen et al. (2011) does not list any uncertainty on the UV flux density, we calculated the standard deviation of the fluxes in the rest-frame 1430–1470 Å waveband on each of the available SDSS DR7 spectra. We assume this as the uncertainty on the rest-frame 2500 Å flux density. We also adopted this method for the 10 sources from the SDSS DR7 (with $z > 5$, hence not included in the catalogue by Shen et al. 2011) and DR12, for which we extrapolated the UV flux density with a fixed slope. This method provides an average uncertainty of 22% over the entire sample of 43 quasars observed within the SDSS releases.

For the quasars at $z > 5.5$, we do not have an estimate of the uncertainty on the rest-frame 2500 Å flux density. The optical spectra we found in the literature for these objects (references in Table A.1) have a comparable, if not higher, signal-to-noise ratio with respect to SDSS. We thus considered a 22% uncertainty on the rest-frame 2500 Å flux density similarly to what we assumed for the entire sample.

5. Relation between $L_{2\,keV}$ and $L_{2500\,Å}$

The non-linear relation between the X-rays (L_X) and UV (L_{UV}) luminosities can be parametrised as

$$\log(L_X) = \beta + \gamma \log(L_{UV}), \quad (1)$$

where β is a normalisation constant and γ is the observed slope. Expressing the luminosities in terms of fluxes and distances, i.e. $L = F4\pi D_L^2$, we obtain

$$\log(F_X) = \beta + \gamma \log(F_{UV}) - (\gamma - 1)\log(4\pi D_L^2), \quad (2)$$

where F_X, F_{UV}, and D_L are the X-ray, UV flux densities, and, luminosity distance, respectively. To perform the analysis of the relation, we considered the following likelihood function:

$$p_i(F_X|F_{X,est}) = \prod_i \frac{1}{\sqrt{2\pi s_i^2}} \exp\left[-\frac{(F_X - F_{X,est})^2}{2s_i^2}\right], \quad (3)$$

where F_X is the rest-frame 2 keV flux estimated as described in Sect. 3, while $F_{X,est}$ is that estimated using Eq. (2) for a given UV flux, and $s_i^2 = \sigma_{UV,i}^2 + \sigma_{X,i}^2 + \delta_{intr}^2$, where δ_{intr} is the intrinsic dispersion, $\sigma_{UV,i}$ and $\sigma_{X,i}$ are the uncertainties on the UV and X-ray fluxes, respectively. To perform the fitting procedure, we used the PYTHON package `emcee` (Foreman-Mackey et al. 2013), which is an implementation of the affine invariant Markov chain Monte Carlo (MCMC) ensemble sampler by Goodman & Weare. Following the approach developed by our group in previous works, we further cleaned the sample on the basis of the X-ray properties and tested the effects of these cuts on the shape of the L_X–L_{UV} relation. We excluded the sources for which the rest-frame 2 keV flux estimate was an upper limit (9 out of 53 objects), and the quasars showing X-ray spectra that were too steep or too flat. Regarding the latter criterion, we excluded the 13 quasars showing an X-ray spectral slope which differs significantly from the peak values of the distribution of photon index for bright, unobscured quasars, i.e. $\Gamma_X = 1.9$–2.0 (e.g. Bianchi et al. 2009). The peculiar slope could suggest either intrinsic obscuration (i.e. $\Gamma_X < 1.5$, which is rare to observe as intrinsic photon index) or an extreme object (i.e. $\Gamma_X > 2.8$). These criteria were applied to avoid the presence of possible contaminants (e.g. absorbed quasars) and to maintain the sample as homogeneous as possible.

The results of the analysis of the L_X–L_{UV} relation on the cleaned sample, consisting of 31 sources with redshift $4.01 < z < 7.08$, are: $\gamma = 0.53^{+0.11}_{-0.11}$, $\beta = 27.46^{+0.05}_{-0.05}$, and $\delta_{intr} = 0.20^{+0.04}_{-0.04}$ dex. These results are fully consistent with the observed slope in other literature works at various redshifts (e.g. Vagnetti et al. 2013, 2010; Lusso & Risaliti 2016 and Nanni et al. 2017) and with samples selected upon different criteria. As said in Sect. 4, we obtained the rest-frame 2500 Å flux density for objects with redshifts $z > 5.5$ from different telescopes, and that could be a further source of dispersion owing to potential cross-normalisation uncertainties within different facilities. In this regard, we excluded SDSS 0231-0728, which has been observed within the SDSS DR12, but owing to the combination of its redshift ($z = 5.41$) and the limited coverage of the SDSS z band (which covers up to ~9200 Å), has an unreliable estimate of the optical flux. Because of the limited SDSS coverage for quasars at redshift higher than about 5, we decided to perform the whole analysis by excluding these sources (9 objects), leading to a subsample of 22 quasars covering the range $4.01 < z < 5.3$. The results of the analysis, considering this subsample, are $\gamma = 0.55^{+0.14}_{-0.14}$, $\beta = 27.43^{+0.05}_{-0.05}$ and $\delta_{intr} = 0.19^{+0.05}_{-0.05}$ dex. Since the results are fully consistent with those obtained with the sample extending up to the highest redshift, we can conclude that the potential dispersion introduced by including optical flux estimates from different instruments is negligible with respect to others; large uncertainties affect the X-ray fluxes, for instance. It is important to note that the intrinsic dispersion obtained using the cleaned sample with and without the cut at redshift $z = 5.3$ is consistent with that found in similarly cleaned quasar samples at lower redshift (e.g. Lusso & Risaliti 2016); this value is lower with respect to what has previously been reported in the literature (e.g. Lusso et al. 2010; Young et al. 2010). This supports the hypothesis that the real intrinsic dispersion can be reduced once an accurate source selection is applied and the sample is made as homogeneous as possible.

Then, we tested the effects of the inclusion of different subsamples on the slope on the L_X–L_{UV} relation. First, we extended the sample to the sources with a flatter or steeper X-ray photon index, where the former class are those that can be affected by intrinsic obscuration; this effect has been observed in a significant fraction of quasars optically classified as unobscured (e.g. Merloni et al. 2014). Including the sources with $1.3 < \Gamma_X < 2.8$, the observed slopes are $\gamma = 0.55^{+0.15}_{-0.15}$ for the quasars with $z < 5.3$ (28/53) and $\gamma = 0.51^{+0.12}_{-0.12}$ for those without any cut in redshift (38/53), respectively. In both cases, the intrinsic dispersion increases (0.22 and 0.23, respectively) with respect to the analysis performed on the cleaned sample. Similarly, including in the cleaned sample the quasars for which we can estimate at most an upper limit to the X-ray flux density, we get $\gamma = 0.62^{+0.15}_{-0.15}$ and $\delta_{intr} \sim 0.19$ for 31 sources with a redshift cut at $zx = 5.3$. Then, considering the 41 quasars covering the entire redshift range $4.01 < z < 7.08$, we get $\gamma = 0.58^{+0.12}_{-0.12}$ and $\delta_{intr} \sim 0.23$. We can conclude that the inclusion of these two subsamples does not affect significantly the shape of the L_X–L_{UV} relation, but only

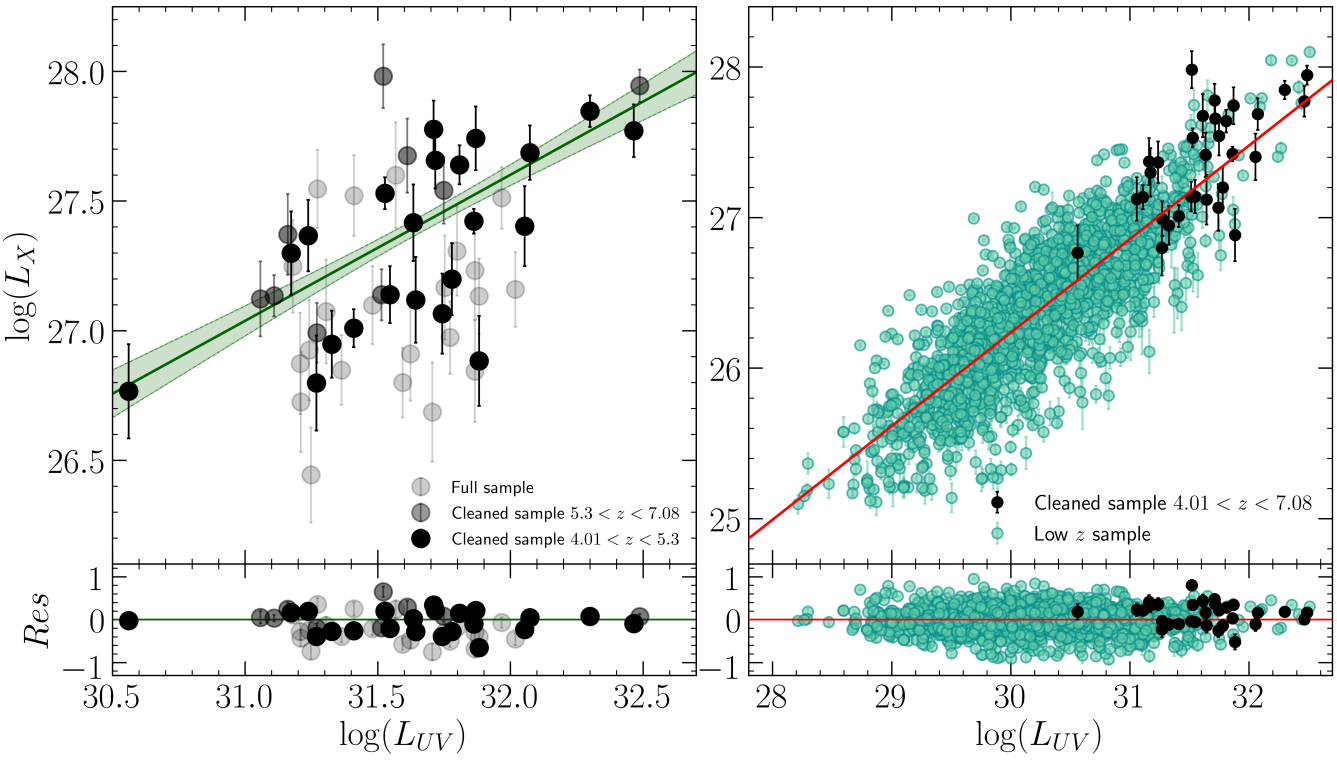

Fig. 3. *Left panel*: $\log(L_X)$ vs. $\log(L_{UV})$ plot for the high-redshift quasars sample ($z > 4$), where L_X and L_{UV} are the monochromatic luminosities at rest-frame 2 keV and 2500 Å in units of in erg s^{-1} Hz^{-1}, respectively. Full black circles indicate the quasars (22 sources) of the cleaned sample with $z < 5.3$, dark grey circles represent those (9) of the cleaned sample with $5.3 < z < 7.08$. The remaining sources, represented with light grey circles, are those excluded owing to the selection criteria adopted, as explained above (e.g. X-ray flux upper limit, X-ray power-law slope Γ_X too steep or too flat). The best-fit parameters obtained from the MCMC regression analysis on the full cleaned sample are represented by the green solid line, while the light green area covers the parameters space between the 16th and 84th percentile ($\gamma = 0.53 \pm 0.11$, $\beta = 27.43 \pm 0.05$, $\delta_{intr} = 0.20 \pm 0.04$, obtained with the sample of 31 objects). On the bottom, the residual between the data and the best-fit model. *Right panel*: $\log(L_X)$ vs. $\log(L_{UV})$ plot. The full cleaned high-redshift sample ($z > 4$) is indicated in black and the sample at lower redshift by Lusso & Risaliti (2016) is indicated in cyan. It is clear that the quasars with $z > 4$ follow the same relation of those at the lowest redshift, suggesting that there is no evolution with cosmic time for the relation. On the bottom, the residual between the data and the model, obtained with the same MCMC regression analysis, on the collection of sources containing both samples represented ($\gamma = 0.62 \pm 0.09$, $\beta = 27.32 \pm 0.16$, $\delta_{intr} = 0.27 \pm 0.04$).

the intrinsic dispersion, which increases. This result is in agreement with those obtained from our group in the previous works on quasar samples at lower redshift, i.e. stricter selection criteria lead to a smaller dispersion resulting from the exclusion of potential contaminants.

The results of the analysis of the L_X–L_{UV} relation, performed on the cleaned sample of 31 sources ($4.01 < z < 7.08$), are presented in the left panel of Fig. 3. In the right panel, the same sources are plotted in the $\log(L_X) - \log(L_{UV})$ plane, along with a sample of similarly selected quasars at lower redshift (~750 objects), presented by Lusso & Risaliti (2016): the high-redshift quasars in this work appear to follow the same relation as those at lower redshift.

6. Summary and conclusions

We presented the results from our study of the non-linear L_X–L_{UV} relation using a sample of 53 high-redshift ($4 < z < 7.08$) unobscured quasars. The observed relation between the X-ray and the UV luminosities indicates the presence of an unknown physical mechanism that links the emission from the accretion disc with that from the X-ray emitting corona. The study of this relation, which has been observed over several orders of magnitude in luminosities and up to high redshift, can provide hints about the nature of this mechanism, placing constraints on the energy generation and transfer in the accretion disc and the surrounding environment in AGN. The main contribution of this work is the use of a carefully selected quasars sample in the highest possible redshift range, the X-ray spectral properties of which were determined through a full spectral analysis, presented in Table A.1 and Fig. C.1. The main results obtained in this work are as follows:

- The observed X-ray spectral properties are consistent with those at lower redshift, for example a mean spectral slope $\Gamma_X = 1.9 \pm 0.5$.
- For the analysis of the relation, we considered only 31 sources, excluding X-ray upper limits, sources with spectra that are too steep or too flat. We observed a dependence ($\gamma = 0.53^{+0.11}_{-0.11}$) which is consistent with that observed at lower redshift ($\gamma \sim 0.6$), hence we find no evolution with the cosmic time.
- The intrinsic dispersion ($\delta_{intr} = 0.20^{+0.04}_{-0.04}$ dex) appears to be lower than in archival works. This is due to the adopted selection criteria, reducing some of the potential systematic effects induced by contaminants, and to the accurate flux estimates, as found in a previous work from our group (Lusso & Risaliti 2016).
- Releasing any of the selection criteria (e.g. including the sources with spectra that are too steep or too flat) leads to a larger intrinsic dispersion.

Our study further supports a non-evolution of the relation between the X-ray and UV luminosities with redshift, suggesting

a universal mechanism linking the emission from the hot corona to that from the accretion disc. Moreover, the non-linearity of the relation provides a new, powerful way to estimate the absolute luminosity, turning quasars into a new class of standard candles. This new class can provide an important contribution in the determination of the cosmological parameters, in particular probing its evolution and expansion in a redshift range that can not be explored using other known observational methods. Indeed, the preliminary results of the work presented have been already used in a Hubble diagram of quasars that was recently published by our group. As shown in recent works from our group (e.g. Risaliti & Lusso 2019; Lusso et al. 2019), cosmological investigations with quasars can be pursued even now.

References

Abazajian, K. N., Adelman-McCarthy, J. K., Agüeros, M. A., et al. 2009, ApJS, 182, 543
Arnaud, K. A. 1996, in Astronomical Data Analysis Software and Systems V, eds. G. H. Jacoby, & J. Barnes, ASP Conf. Ser., 101, 17
Aubourg, É., Bailey, S., Bautista, J. E., et al. 2015, Phys. Rev. D, 92, 123516
Avni, Y., & Tananbaum, H. 1986, ApJ, 305, 83
Betoule, M., Kessler, R., Guy, J., et al. 2014, A&A, 568, A22
Bianchi, S., Guainazzi, M., Matt, G., Fonseca Bonilla, N., & Ponti, G. 2009, A&A, 495, 421
Brandt, W. N., Vignali, C., Schneider, D. P., et al. 2004, Adv. Space Res., 34, 2478
Di Matteo, T. 1998, MNRAS, 299, L15
du Mas des Bourboux, H., Le Goff, J. M., Blomqvist, M., et al. 2017, A&A, 608, A130
Foreman-Mackey, D., Hogg, D. W., Lang, D., & Goodman, J. 2013, PASP, 125, 306
Gallerani, S., Maiolino, R., Juarez, Y., et al. 2010, A&A, 523, A85
Ghirlanda, G., Ghisellini, G., Lazzati, D., & Firmani, C. 2004, ApJ, 613, L13
Haardt, F., & Maraschi, L. 1991, ApJ, 380, L51
Haardt, F., & Maraschi, L. 1993, ApJ, 413, 507
Hjorth, J., Vreeswijk, P. M., Gall, C., & Watson, D. 2013, ApJ, 768, 173
Iwamuro, F., Kimura, M., Eto, S., et al. 2004, ApJ, 614, 69
Jiang, L., Fan, X., Vestergaard, M., et al. 2007, AJ, 134, 1150
Just, D. W., Brandt, W. N., Shemmer, O., et al. 2007, ApJ, 665, 1004
Komatsu, E., Dunkley, J., Nolta, M. R., et al. 2009, ApJS, 180, 330
Lusso, E., & Risaliti, G. 2016, ApJ, 819, 154
Lusso, E., & Risaliti, G. 2017, A&A, 602, A79
Lusso, E., Comastri, A., Vignali, C., et al. 2010, A&A, 512, A34
Lusso, E., Comastri, A., Simmons, B. D., et al. 2012, MNRAS, 425, 623
Lusso, E., Worseck, G., Hennawi, J. F., et al. 2015, MNRAS, 449, 4204
Lusso, E., Piedipalumbo, E., Risaliti, G., et al. 2019, A&A, 628, L4
Merloni, A. 2003, MNRAS, 341, 1051
Merloni, A., Bongiorno, A., Brusa, M., et al. 2014, MNRAS, 437, 3550
Mortlock, D. J., Warren, S. J., Venemans, B. P., et al. 2011, Nature, 474, 616
Nanni, R., Vignali, C., Gilli, R., Moretti, A., & Brandt, W. N. 2017, A&A, 603, A128
Nanni, R., Gilli, R., Vignali, C., et al. 2018, A&A, 614, A121
Pâris, I., Petitjean, P., Ross, N. P., et al. 2017, A&A, 597, A79
Read, A. M., Guainazzi, M., & Sembay, S. 2014, A&A, 564, A75
Risaliti, G., & Lusso, E. 2015, ApJ, 815, 33
Risaliti, G., & Lusso, E. 2019, Nat. Astron., 3, 272
Risaliti, G., Elvis, M., Fabbiano, G., et al. 2007, ApJ, 659, L111
Shakura, N. I., & Sunyaev, R. A. 1973, A&A, 24, 337
Shemmer, O., Brandt, W. N., Vignali, C., et al. 2005, ApJ, 630, 729
Shemmer, O., Brandt, W. N., Schneider, D. P., et al. 2006, ApJ, 644, 86
Shemmer, O., Brandt, W. N., Paolillo, M., et al. 2017, ApJ, 848, 46
Shen, Y., Richards, G. T., Strauss, M. A., et al. 2011, ApJS, 194, 45
Steffen, A. T., Strateva, I., Brandt, W. N., et al. 2006, AJ, 131, 2826
Strateva, I. V., Brandt, W. N., Schneider, D. P., Vanden Berk, D. G., & Vignali, C. 2005, AJ, 130, 387
Svensson, R., & Zdziarski, A. A. 1994, ApJ, 436, 599
Vagnetti, F., Turriziani, S., Trevese, D., & Antonucci, M. 2010, A&A, 519, A17
Vagnetti, F., Antonucci, M., & Trevese, D. 2013, A&A, 550, A71
Vanden Berk, D. E., Richards, G. T., Bauer, A., et al. 2001, AJ, 122, 549
Vignali, C., Brandt, W. N., Fan, X., et al. 2001, AJ, 122, 2143
Vignali, C., Brandt, W. N., & Schneider, D. P. 2003a, AJ, 125, 433
Vignali, C., Brandt, W. N., Schneider, D. P., et al. 2003b, AJ, 125, 2876
Vignali, C., Brandt, W. N., Schneider, D. P., & Kaspi, S. 2005, AJ, 129, 2519
Wu, X.-B., Wang, F., Fan, X., et al. 2015, Nature, 518, 512
Young, M., Elvis, M., & Risaliti, G. 2010, ApJ, 708, 1388

Appendix A: Table

Table A.1. Quasar properties.

Name (1)	RA (2)	DEC (3)	z (4)	$f_{2500Å}$ (5)	Γ_X (6)	$L_{0.5-2\ keV}$ (7)	$L_{2-10\ keV}$ (8)	f_{2keV} (9)	χ^2_{dof} (10)	#dof (11)	t_{exp} (12)	C/X (13)	Ref. (14)
ULAS J1120+0641	11h20m01.48s	+06d41m24.3s	7.08	5.7[1]	$2.0^{+0.4}_{-0.4}$	12^{+4}_{-7}	12^{+3}_{-3}	$1.9^{+1.1}_{-0.8}$	1.16	36	2.3	X	1
SDSS J114816.7+525150.4	11h48m16.65s	+52d51m50.2s	6.43	0.84[2]	$1.5^{+0.5}_{-0.5}$	$3.^{+8}_{-2}$	8^{+5}_{-3}	$1.0^{+1.5}_{-0.6}$	0.47	32	5	X	2
SDSS 1030+0524	10h30m27.10s	+05d24m55.0s	6.31	0.42[3]	$2.1^{+0.2}_{-0.2}$	5^{+7}_{-3}	5^{+3}_{-2}	$7.6^{+2}_{-1.5}$	1.07	156	103.8	X	3
SDSS J010013.0+280225.9	01h00m13.02s	+28d02m55.8s	6.30	6.9[4]	$2.4^{+0.2}_{-0.2}$	100^{+70}_{-40}	59^{+15}_{-12}	14^{+5}_{-4}	1.10	182	65.4	X	4
SDSS 1623+3112	16h23m31.81s	+31d12m00.0s	6.22	0.40[5]	1.9 (†)	< 5	< 4	< 1.8	16.50	7	17.2	C	5
SDSS 1602+4228	16h02m53.98s	+42d28m24.9s	6.07	1.37[5]	$2.0^{+0.5}_{-0.5}$	23^{+47}_{-16}	28^{+15}_{-10}	6^{+7}_{-3}	1.00	26	13.2	C	5
SDSS 1630+4012	16h30m33.90s	+40d12m09.6s	6.05	0.28[2]	$2.0^{+0.7}_{-0.7}$	9^{+30}_{-7}	10^{+7}_{-4}	$2.3^{+4}_{-1.5}$	1.36	16	27.3	C	2
SDSS 1306+0356	13h06m08.26s	+03d56m26.3s	5.99	0.32[6]	$1.9^{+0.2}_{-0.2}$	8^{+6}_{-3}	13^{+3}_{-2}	$2.8^{+1.2}_{-0.8}$	0.79	91	119.7	C	6
SDSS 1411+1217	14h11m11.29s	+12d17m37.4s	5.93	0.37[6]	$2.3^{+0.8}_{-0.8}$	$18^{+90}_{-15.0}$	16^{+-8}_{-8}	5^{+8}_{-3}	1.34	13	14.4	C	6
SDSS 0836+0054	08h36m43.85s	+00d54m53.3s	5.82	1.10[6]	$1.9^{+0.5}_{-0.5}$	30^{+60}_{-20}	48^{+25}_{-18}	10^{+11}_{-6}	0.96	24	5.7	C	6
SDSS 0231−0728	02h31m37.65s	-07d28m54.5s	5.41	1.24(⋆)	$2.1^{+0.6}_{-0.5}$	$1.80^{+2.0}_{-1.0}$	70^{+30}_{-20}	20^{+20}_{-11}	1.08	20	4.2	C	7
SDSS 1053+5804	10h53m22.99s	+58d04m12.1s	5.21	1.51 (⋆)	1.9 (†)	< 0.8	< 20	< 8.4	0.98	4	4.7	C (*)(△)	7
SDSS 2228−0757	22h28m45.15s	-07d57m55.4s	5.14	0.68 (⋆)	1.9 (†)	< 0.1	< 4	< 2.3	2.10	3	7.0	C	7
SDSS 0756+4104	07h56m18.14s	+41d04m08.6s	5.09	0.74 (⋆)	$1.8^{+0.7}_{-0.6}$	$1.0^{+1.0}_{-0.6}$	22^{+13}_{-9}	5^{+7}_{-3}	2.36	18	7.4	C	7
SDSS 1204−0021	12h04m41.73s	-00d21m49.6s	5.03	1.94 (⋆)	$1.7^{+1.1}_{-1.2}$	$0.6^{+1.0}_{-0.5}$	13^{+8}_{-6}	3^{+6}_{-2}	0.33	9	6.3	C	7
SDSS J133422.63+475033.6	13h34m22.64s	+47d50m33.6s	5.00	2.4	$1.9^{+0.6}_{-0.6}$	$0.8^{+1.0}_{-0.5}$	14^{+8}_{-6}	4^{+5}_{-2}	1.31	18	11.6	C	7
SDSS 2216+0013	22h16m44.00s	+00d13m48.3s	4.99	0.67 (⋆)	$2.3^{+1.1}_{-1.0}$	$0.8^{+2.0}_{-0.6}$	10^{+10}_{-6}	5^{+10}_{-3}	0.64	7	7.5	C	8
SDSS 0040−0915	00h40m54.65s	-09d15m26.8s	4.98	2.5 (⋆)	$1.6^{+1.2}_{-0.7}$	6^{+30}_{-5}	13^{+10}_{-7}	$3^{+6}_{-1.9}$	1.07	139	(‡)	X	7
SDSS 1026+4719	10h26m22.87s	+47d19m07.2s	4.94	2.9	$1.3^{+1.1}_{-1.1}$	$0.9^{+5}_{-0.8}$	25^{+39}_{-17}	4^{+20}_{-4}	1.12	5	2.3	C (△)	7
SDSS 1536+5008	15h36m50.26s	+50d08m10.3s	4.93	3.0	$1.3^{+0.6}_{-0.6}$	$1.8^{+1.0}_{-0.7}$	27^{+13}_{-10}	3^{+5}_{-2}	1.77	14	4.6	C	7
SDSS J105123.04+354534.3	10h51m23.04s	+35d45m34.3s	4.91	3.7	$1.3^{+0.3}_{-0.3}$	14^{+20}_{-8}	46^{+24}_{-17}	8^{+8}_{-4}	1.34	62	(‡)	X	7
SDSS J142103.83+343332.0	14h21m03.83s	+34d33m32.0s	4.90	2.0	1.9 (†)	< 0.1	< 3	< 1.3	5.68	4	12.9	C	7
SDSS J173744.88+582829.62	17h37m44.88s	+58d28m29.6s	4.89	2.9	1.9 (†)	< 0.1	< 3	< 1.7	4.16	1	4.6	C	7
SDSS 2225−0014	22h25m09.20s	-00d14m06.9s	4.89	2.3	1.9 (†)	< 0.7	< 7	< 3.5	2.65	2	3.4	C	7
SDSS 1023+6335	10h23m32.07s	+63d35m08.0s	4.88	0.75	$1.6^{+1.2}_{-1.1}$	$0.4^{+1.0}_{-0.3}$	7^{+8}_{-4}	$1.5^{+5}_{-1.3}$	0.66	4	4.7	C	7
SDSS 0211−0009	02h11m02.70s	-00d09m10.3s	4.87	0.17 (⋆)	$1.7^{+1.2}_{-1.1}$	$0.4^{+1.0}_{-0.3}$	6^{+7}_{-4}	$1.4^{+4}_{-1.2}$	2.76	4	4.9	C	8
SDSS 0951+5945	09h51m51.19s	+59d45m56.2s	4.86	0.83	1.9 (†)	< 0.8	< 10	< 3.5	5.45	3	5.1	C	7
SDSS J075652.07+450258.86	07h56m52.08s	+45d02m58.9s	4.83	0.68	1.9 (†)	< 5	< 40	< 2.1	9.20	3	7.0	C	7
SDSS 0941+5947	09h41m08.36s	+59d47m25.7s	4.82	1.78	$1.3^{+1.3}_{-1.1}$	$0.8^{+5.0}_{-0.7}$	14^{+30}_{-9}	$2.0^{+6}_{-1.7}$	1.65	11	4.2	C	7
SDSS J142705.86+330817.9	14h27m05.86s	+33d08m18.0s	4.71	2.8	$1.6^{+1.0}_{-0.9}$	$1.5^{+5.}_{-1.2}$	21^{+25}_{-13}	5^{+16}_{-4}	3.98	8	5.0	C(△)	7
PSS 1347+4956	13h47m43.29s	+49d56m21.3s	4.51	5.8	$2.14^{+0.5}_{-0.5}$	5^{+4}_{-2}	34^{+12}_{-9}	13^{+10}_{-6}	0.77	28	5.9	C	7
SDSS 1302+0030	13h02m16.13s	+00d30m32.1s	4.50	0.87	1.9 (†)	< 0.8	< 7	< 1.5	3.91	2	10.8	C	7
PSS 0808+5215	08h08m49.43s	+52d15m15.3s	4.44	3.8	$1.5^{+1.0}_{-1.0}$	$0.7^{+2.0}_{-0.6}$	9^{+8}_{-5}	$2.1^{+5}_{-1.7}$	1.70	7	4.9	C	7
BRI 0103+0032	01h06m19.24s	+00d48m23.3s	4.44	3.7	$2.0^{+0.7}_{-0.6}$	5^{+6}_{-3}	43^{+18}_{-14}	15^{+16}_{-8}	3.44	20	3.7	C	7

Table A.1. continued.

Name (1)	RA (2)	DEC (3)	z (4)	$f_{2500\,\text{Å}}$ (5)	Γ_X (6)	$L_{0.5-2\,\text{keV}}$ (7)	$L_{2-10\,\text{keV}}$ (8)	$f_{2\,\text{keV}}$ (9)	$\chi^2_{\text{d.o.f.}}$ (10)	$\#_{\text{d.o.f.}}$ (11)	t_{exp} (12)	C/X (13)	Ref. (14)
SDSS 0831+5235	08h31m03.01s	+52d35m33.5s	4.44	1.78	$2.0^{+0.4}_{-0.5}$	9^{+8}_{-4}	9^{+2}_{-2}	$3.8^{+1.5}_{-1.8}$	1.02	502	(‡)	X	7
PSS 1443+2724	14h43m31.18s	+27d24m36.8s	4.44	2.2	$1.9^{+0.8}_{-0.9}$	3^{+4}_{-2}	23^{+15}_{-10}	7^{+11}_{-5}	4.23	8	2.2	C	7
SDSS 1401+0244	14h01m46.53s	+02d44m34.7s	4.44	3.7	$1.6^{+0.2}_{-0.2}$	12^{+4}_{-3}	26^{+3}_{-3}	$7.3^{+1.5}_{-1.4}$	1.19	613	(‡)	X	7
PSS 0747+4434	07h47m49.74s	+44d34m17.0s	4.43	1.31	$3.0^{+1.3}_{-1.1}$	$1.3^{+1.0}_{-0.6}$	10^{+8}_{-5}	9^{+16}_{-7}	1.35	6	4.5	C	7
BR 1600+0724	16h03m20.89s	+07d21m04.5s	4.38	5.9	$2.6^{+1.1}_{-1.0}$	3^{+5}_{-23}	12^{+10}_{-6}	7^{+12}_{-5}	3.78	6	4.6	C	7
SDSS 2357+0043	23h57m18.36s	+00d43m50.4s	4.36	1.22	$1.4^{+0.6}_{-0.6}$	$0.7^{+1.0}_{-0.4}$	9^{+5}_{-3}	$2.0^{+3}_{-1.2}$	2.43	18	12.8	C	7
PSS 1317+3531	13h17m43.13s	+35d31m31.8s	4.34	0.79	$2.9^{+2.5}_{-1.8}$	$2.0^{+8.0}_{-1.8}$	7^{+8}_{-5}	5.0^{+14}_{-4}	0.39	2	2.8	C	7
PSS 0955+5940	09h55m11.33s	+59d40m30.6s	4.34	3.5	$1.8^{+0.9}_{-0.9}$	5^{+3}_{-2}	31^{+7}_{-6}	5^{+6}_{-3}	1.53	11	43.6	C	7
SDSS 0050−0053	00h50m06.35s	−00d53m19.3s	4.33	3.2	$1.4^{+0.7}_{-0.7}$	$0.8^{+1.0}_{-0.6}$	12^{+5}_{-4}	$2.7^{+3}_{-1.7}$	2.39	21	13.1	C	7
PSS 0957+3308	09h57m44.46s	+33d08m20.8s	4.20	6.0	$1.3^{+0.9}_{-0.9}$	$1.6^{+3.0}_{-1.1}$	20^{+8}_{-7}	4^{+6}_{-3}	0.59	16	6.1	C	7
PSS 0059+0003	00h59m22.66s	+00d03m01.4s	4.18	1.77	$1.3^{+0.7}_{-0.7}$	$1.4^{+3.0}_{-1.0}$	17^{+12}_{-8}	4^{+6}_{-3}	3.13	10	2.7	C	7
SDSS 1444−0123	14h44m28.63s	−01d23m44.0s	4.18	1.10	$4.1^{+2.2}_{-1.5}$	3^{+16}_{-2}	7^{+6}_{-4}	11^{+19}_{-7}	3.87	29	10.1	C	7
PSS 0133+0400	01h33m40.30s	+04d00m59.9s	4.15	2.3 (⋆)	$1.9^{+0.2}_{-0.2}$	$4.2^{+1.0}_{-1.1}$	30^{+5}_{-4}	10^{+3}_{-3}	1.06	136	65.0	C	8
PSS 0209+0517	02h09m44.59s	+05d17m13.3s	4.14	3.7 (⋆)	$2.4^{+0.6}_{-0.6}$	6^{+5}_{-3}	26^{+10}_{-8}	14^{+11}_{-7}	1.60	21	5.8	C	8
PSS 1057+4555	10h57m56.26s	+45d55m53.0s	4.14	17.5	$2.0^{+0.6}_{-0.5}$	8^{+6}_{-3}	48^{+16}_{-13}	18^{+12}_{-8}	3.87	29	2.8	C	7
PSS 1326+0743	13h26m11.85s	+07d43m58.4s	4.09	12.0	$1.8^{+0.3}_{-0.3}$	9^{+3}_{-2}	55^{+12}_{-10}	19^{+8}_{-6}	0.89	57	⋄	C	7
SDSS 1413+0000	14h13m15.37s	+00d00m32.4s	4.08	1.32	$1.7^{+0.6}_{-0.6}$	$1.4^{+2.0}_{-0.9}$	10^{+5}_{-4}	$2.8^{+3}_{-1.6}$	1.48	19	12.5	C	7
SDSS J111812.91+441122.3	11h18m12.91s	+44d11m22.3s	4.02	1.65	$1.5^{+0.6}_{-0.6}$	5^{+3}_{-2}	12^{+2}_{-2}	$3.3^{+1.1}_{-1.0}$	1.13	600	(‡)	X	7
SDSS 1408+0205	14h08m50.91s	+02d05m22.7s	4.01	3.3	$2.2^{+0.6}_{-0.6}$	9^{+8}_{-4}	41^{+14}_{-11}	19^{+16}_{-9}	0.76	29	6.0	C	7

Notes. Columns: (1) Source name. (2) Right ascension (RA) in the *J2000* frame. (3) Declination (Dec) in the *J2000* frame. (4) Archival source redshift. (5) Rest-frame 2500 Å flux density, in unity of 10^{-28} erg s^{-1} cm^{-2} Hz^{-1}. Uncertainties are assumed to be about the 22% of the flux. See Sect. 4 for details. (6) Rest-frame 0.5–2 keV luminosity in units of 10^{44} erg s^{-1}. (7) Rest-frame 2–10 keV luminosity in units of 10^{44} erg s^{-1}. (8) X-ray spectral photon index, evaluated through the fitting procedure (see Sect. 3). (9) Rest-frame 2 keV flux density, in unity of 10^{-32} erg s^{-1} cm^{-2} Hz^{-1}. See Sect. 3 for details. (10) Reduced χ^2 of the X-ray spectral fit procedure. (11) Number of degrees of freedom in the X-ray spectral fit, i.e. the number of spectral bins minus the number of the free parameters. For the detected sources, the free parameters are the power-law slope and normalisation. (12) Exposure time of the X-ray observation in units of ks. (13) Telescope used for this observation: *C* for *Chandra*, *X* for *XMM-Newton*. (⋆)Extrapolation of the rest-frame 2500 Å flux density through fixed slope on SDSS DR7 or DR12 data. Numbers in column 5: Extrapolation through a fixed slope on archival observations: (1) Mortlock et al. 2011, (2) Iwamuro et al. 2004, (3) Hjorth et al. 2013, (4) Wu et al. 2015, (5) Gallerani et al. 2010, (6) Jiang et al. 2007, (7) Shen et al. 2011, (8) Pâris et al. 2017. (†)Upper limit on X-ray monochromatic flux estimate. (∗)Off-axis sources. (△)Sources detected using ACIS-I camera. All of the others were observed using ACIS-S. (‡)Multiple X-ray observations fitted together.

Appendix B: Extrapolation of the 2500 Å flux density

We present the procedure adopted to choose the best method to infer the rest-frame 2500 Å flux density for the sources with the SDSS (DR7 or DR12) but not included in the catalogue by Shen et al. (2011). Given the redshift of the sources in this sample, the rest-frame 2500 Å is outside of the spectral coverage for SDSS DR7 and DR12. We compared the following methods to extrapolate this value: 1) from the 1450 Å flux density, using a fixed slope $S_\nu \propto \nu^{-\alpha}$ with $\alpha = 0.5$ (see Vanden Berk et al. 2001); 2) from the same using a slope $\alpha = 0.79$ (see Vignali et al. 2001); and 3) from the fit to the source spectrum to use the continuum slope extrapolate the 2500 Å flux. To verify whether the 2500 Å flux density values obtained with these methods are reliable, we performed the following test. We selected 30 luminous quasars at redshift $z = 2$, fulfilling the selection criteria applied to the main sample, i.e. unobscured (type I) optically selected quasars, classified as radio quiet sources, which show no BAL features. For these sources the rest-frame 2500 Å flux density falls well within the SDSS spectral coverage, and we can give a reliable measure of this quantity with a procedure similar to that performed by Shen et al. (2011) (i.e. continuum, FeII, and emission lines spectral fitting). We then assumed the redshift of the source to be higher than the true one, i.e. we shifted the wavelength axis to the source rest-frame and "cut" it at the highest observable wavelength according to the assumed redshift and the SDSS wavelength coverage, performed the fit again, and extrapolated the flux density at 2500 Å. We carried out this analysis for several values of redshift ($z = 3$, 4, 4.2, 4.4, 4.6, 4.8, 5.0, 5.2) and then compared the extrapolated 2500 Å flux with the true value. This comparison is shown in Fig. B.1. The extrapolated 2500 Å flux densities are in good agreement with the true values. The extrapolation using the constant slope $\alpha = 0.50$ turns out to be more accurate than other methods at redshift higher $z > 4.4$ (on the basis of the observed dispersion). We also adopted the extrapolation of the flux density with the constant slope $\alpha = 0.50$ for the sources not covered with an SDSS observation, but for which data from other facilities were available in the literature.

We also checked the consistency of the UV flux density estimates by Shen et al. (2011) with that obtained with the extrapolation with a fixed slope $\alpha = 0.5$ (i.e. the first method described above) from the SDSS DR7 spectra for the 33 sources. We found that the two different estimates are fully consistent within the uncertainty (assumed of 22%) for almost the entire sample. Only a couple of sources showed a significant discrepancy (larger than 2σ): there are many reasons for this, for example, a wrong fit from the automatic procedure by Shen et al. (2011) or, equivalently, a significant discrepancy between the assumed slope in the extrapolation (i.e. $\alpha = 0.5$) and the intrinsic continuum slope of this particular sources. However, we tested whether the inclusion or not of these sources could affect the best-fit parameters of the L_X–L_{UV} relation and we found that they are not statistically significant (i.e. we found fully consistent results in the two cases); then we included them in the sample.

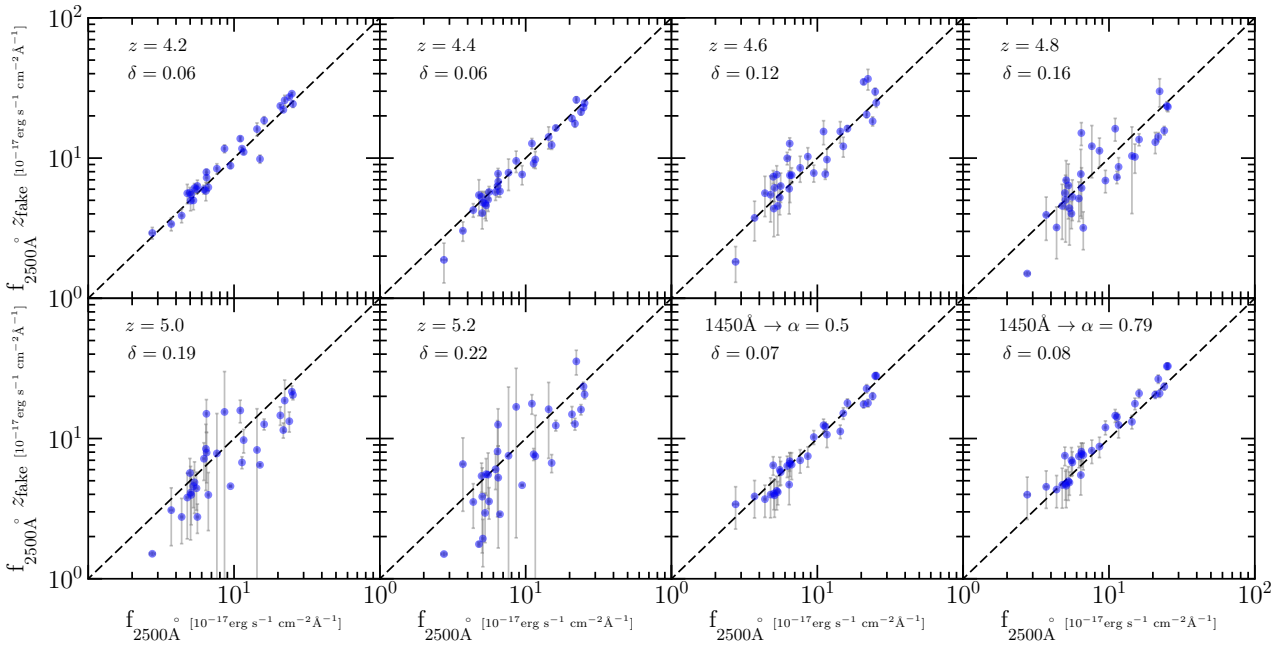

Fig. B.1. Results of the simulations used to choose between different procedures to estimate the 2500 Å flux densities on 30 luminous quasars at $z \simeq 2$. We compared the flux density observed values with those obtained with each of the three methods described in the appendix. *From the top left panel*: rest-frame 2500 Å flux estimated assuming redshift 4.2, 4.4, 4.6, 4.8, 5.0, 5.2 (y-axis) vs. that estimated from the full spectrum (x-axis). The last two panels represent the comparison between the true rest-frame 2500 Å flux from the spectra, and that estimated from an extrapolation with a fixed power law, having the slope equal to 0.5 (Vanden Berk et al. 2001) and 0.79 (Vignali et al. 2001), respectively. The normalisation is assumed to be in the 1430−1470 Å spectral range.

Appendix C: X-ray spectral analysis

We present the X-ray spectra for 41 sources in the sample for which we performed the spectral fit with the exclusion of the 3 spectra presented in Sect. 3.2; the sources for which we can only estimate an upper limit to the X-ray fluxes are not included. The sources are listed with increasing redshift. The spectra, binned to a 90% significance level for presentation purposes, are presented in the top panel along with the best-fit model (Galactic absorption and a power law), while the bottom panel shows the residuals, data minus model, in units of sigma. The observed-frame energies, in units of kilo electron volts, are represented in the x-axes.

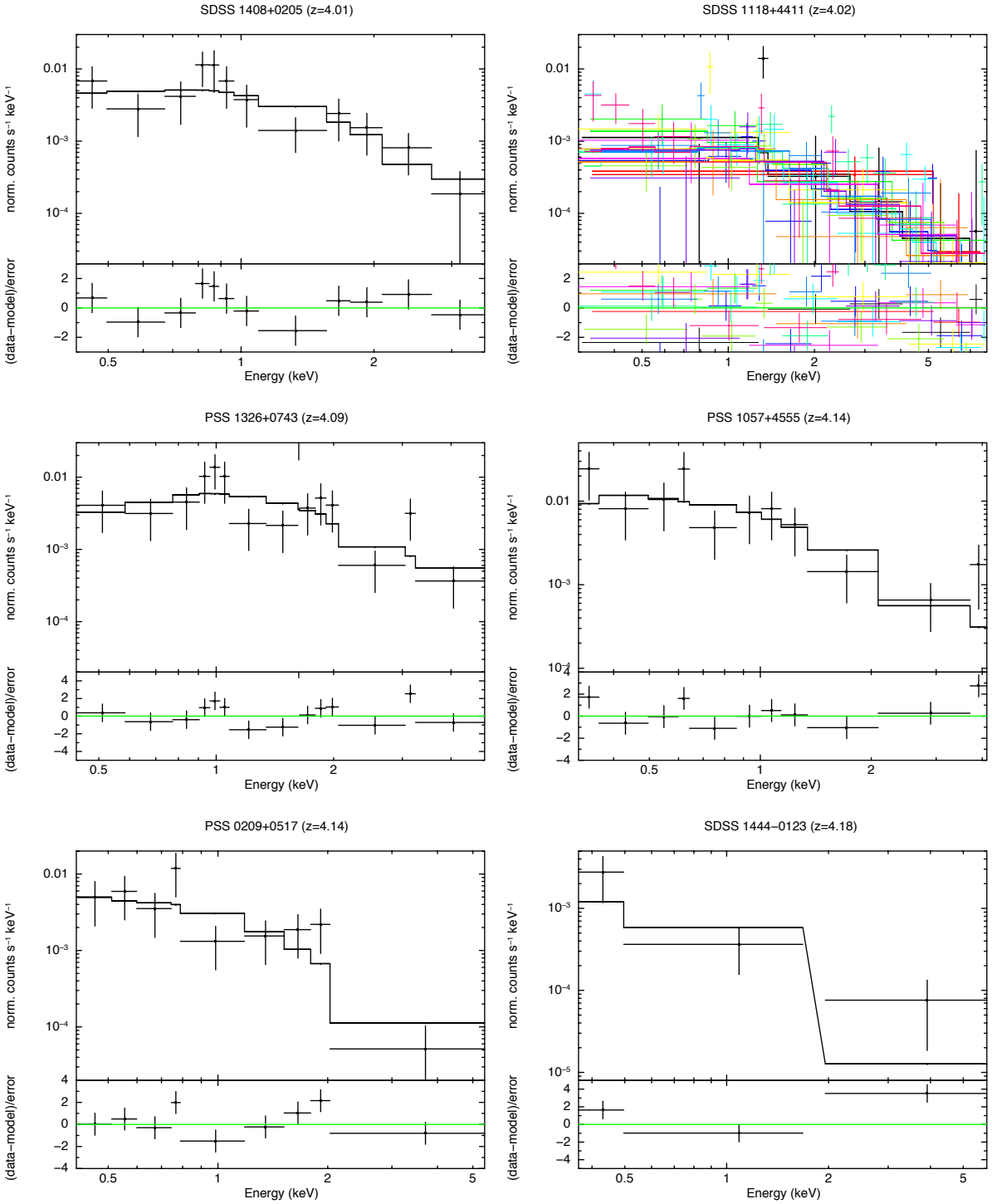

Fig. C.1. Best-fit models and data for 41 sources are presented in the *top panels*. Single epoch *Chandra* data are represented with black crossed points, while the best-fit model is indicated by a black line. In case of multiple *Chandra* data, we chose the more representative observation (e.g. the longest, or the observation for which we have the best-fit model with the lowest $\chi^2_{d.o.f.}$). In case of single epoch *XMM-Newton* data, EPIC-pn data are indicated in black and merged EPIC-MOS in red. Multiple *XMM-Newton* observations have EPIC-pn and merged EPIC-MOS in various colours.

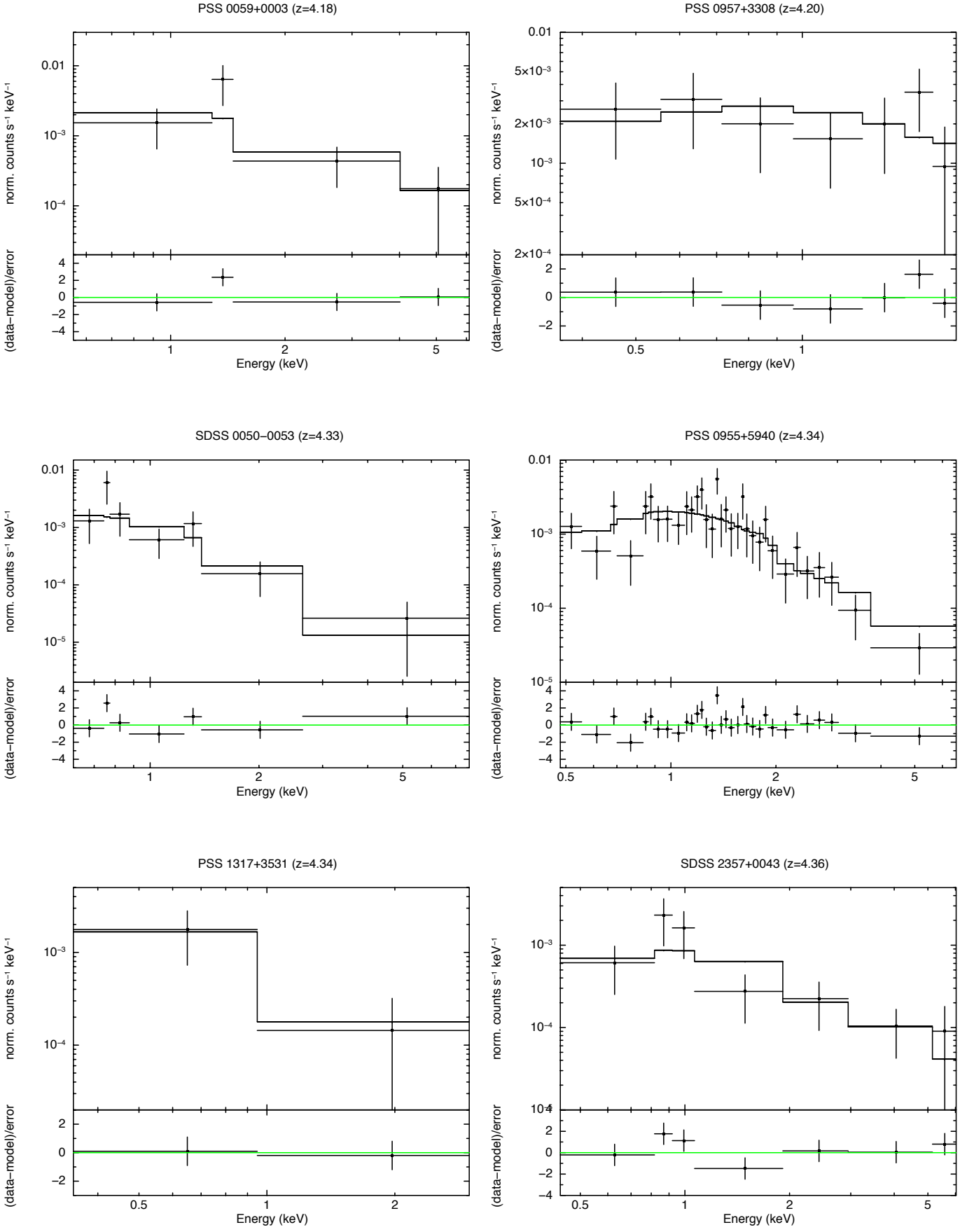

Fig. C.1. continued

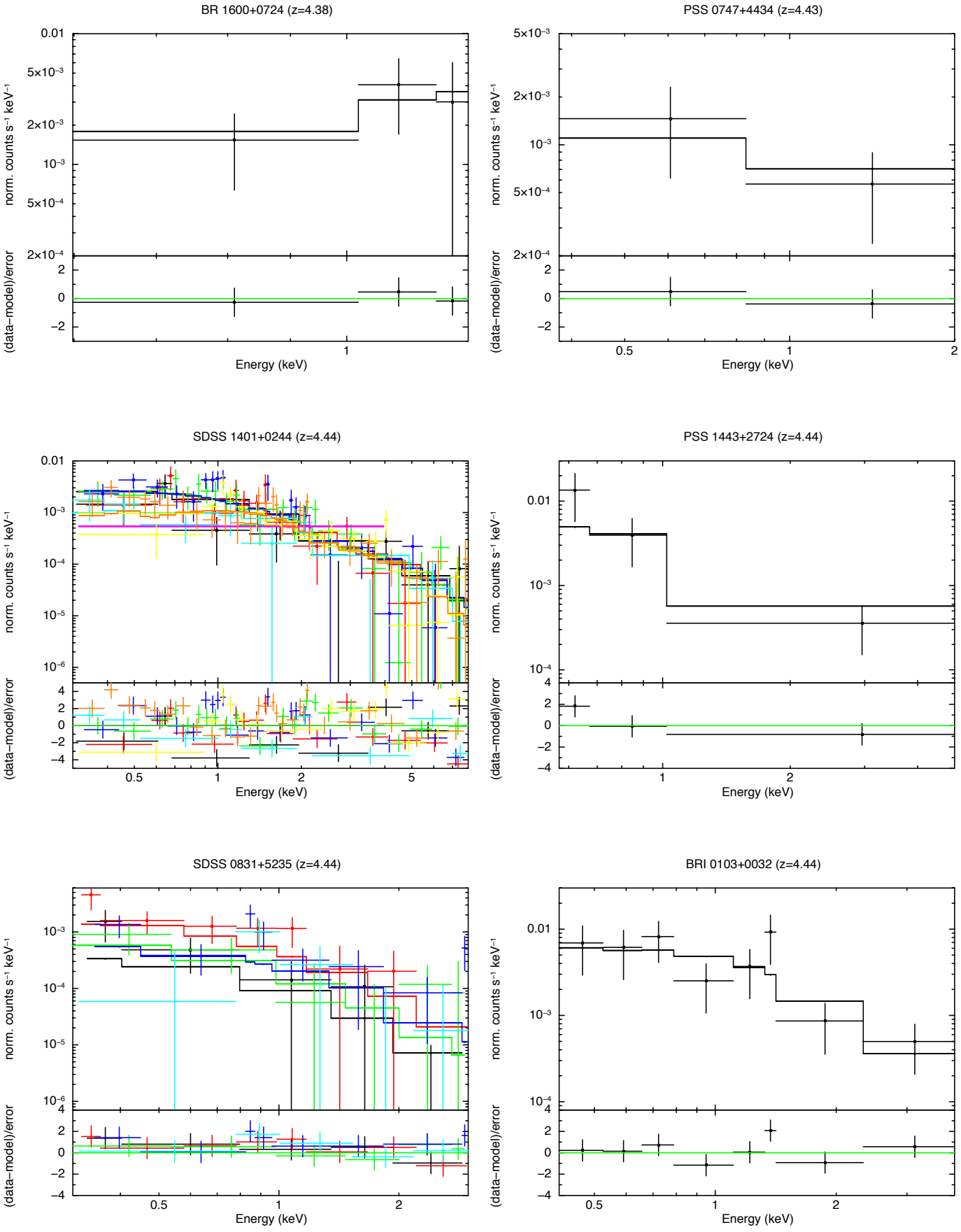

Fig. C.1. continued

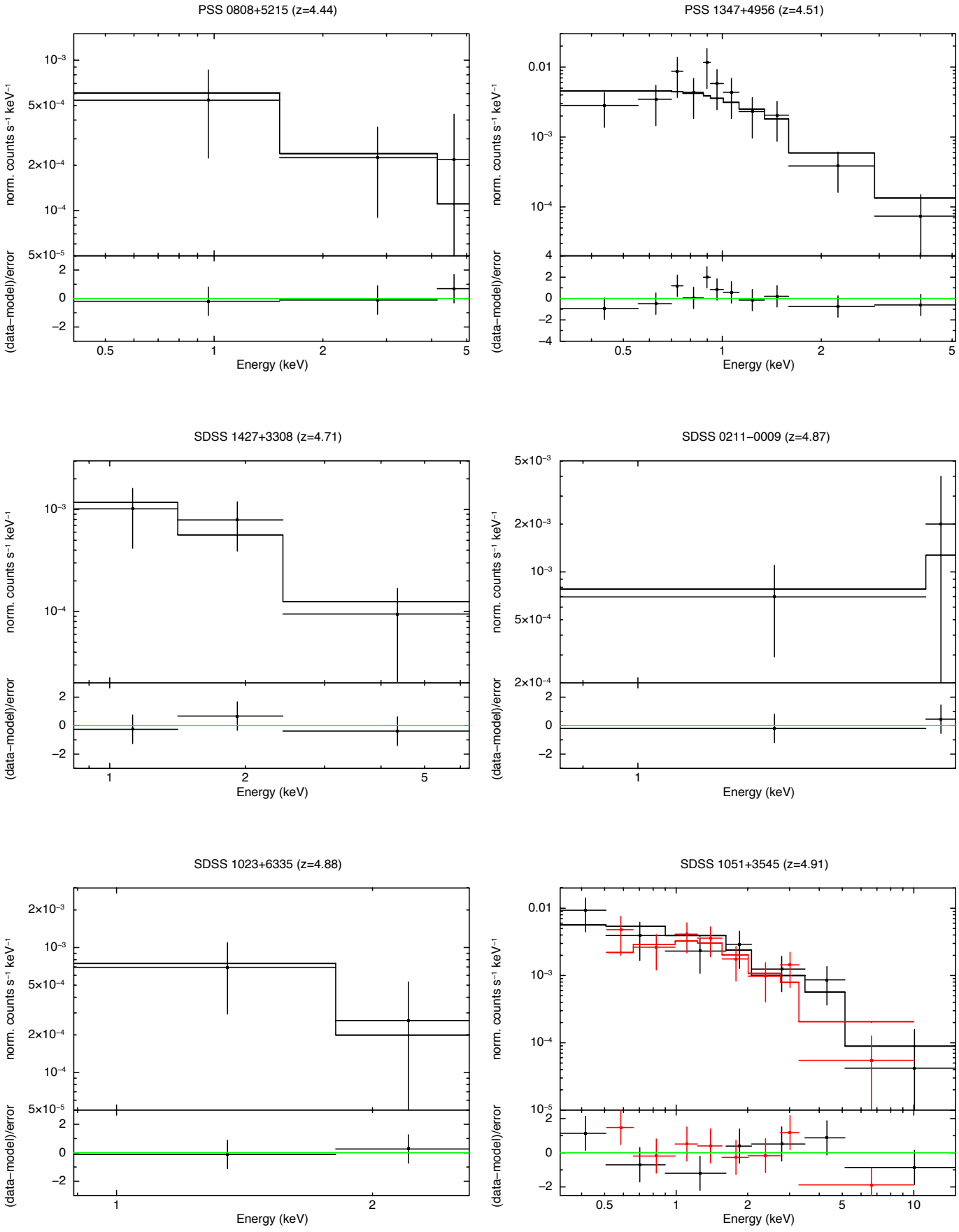

Fig. C.1. continued

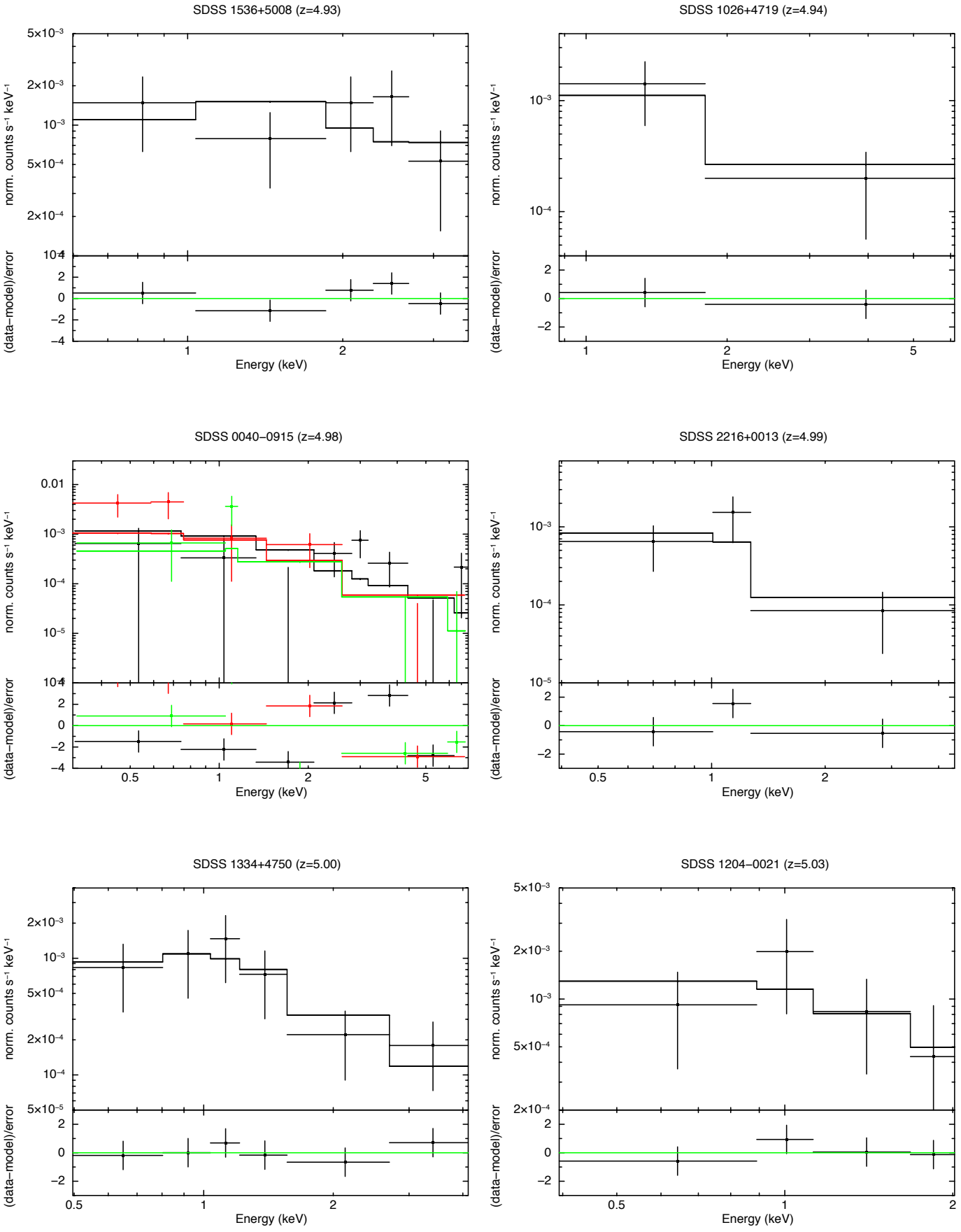

Fig. C.1. continued

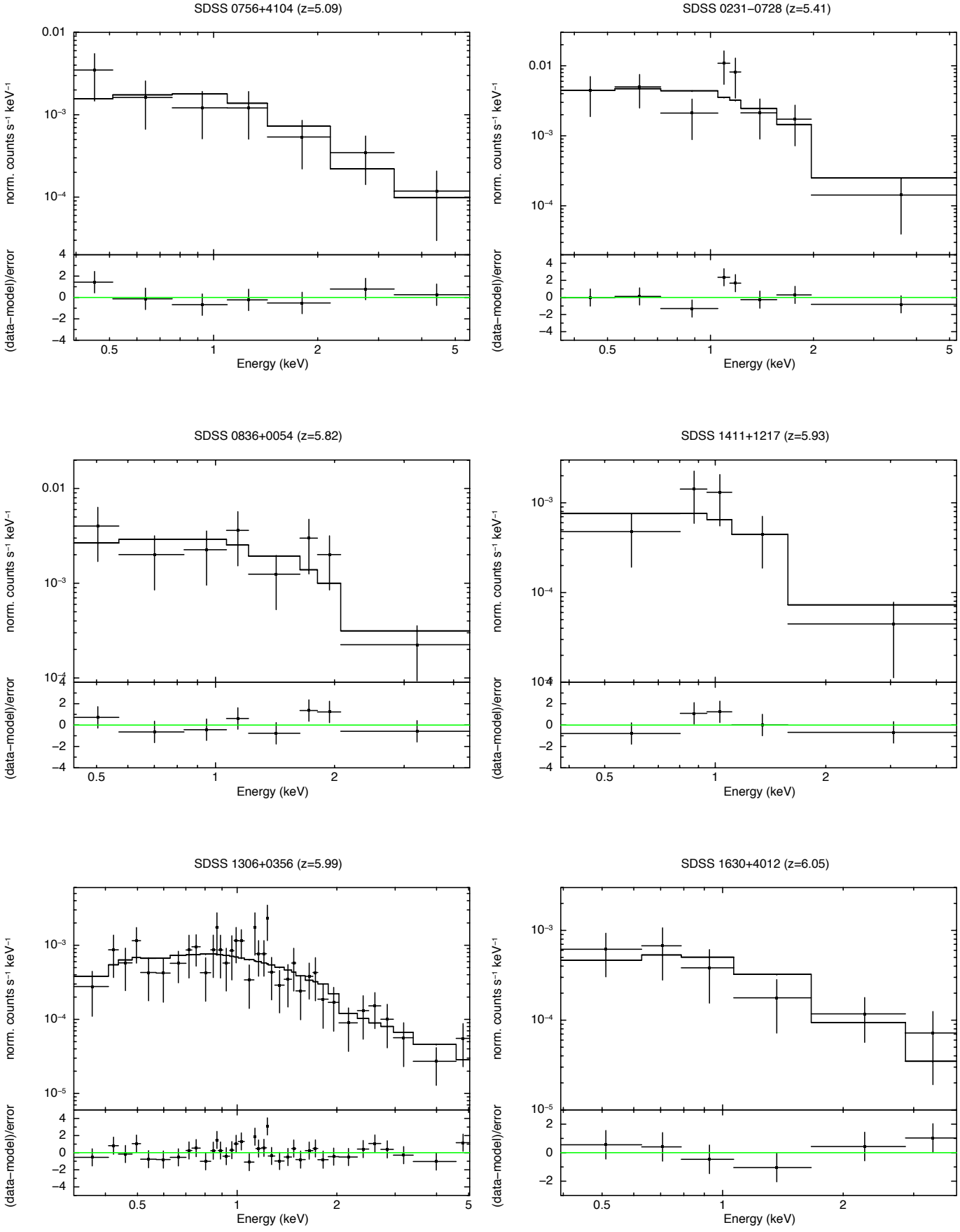

Fig. C.1. continued

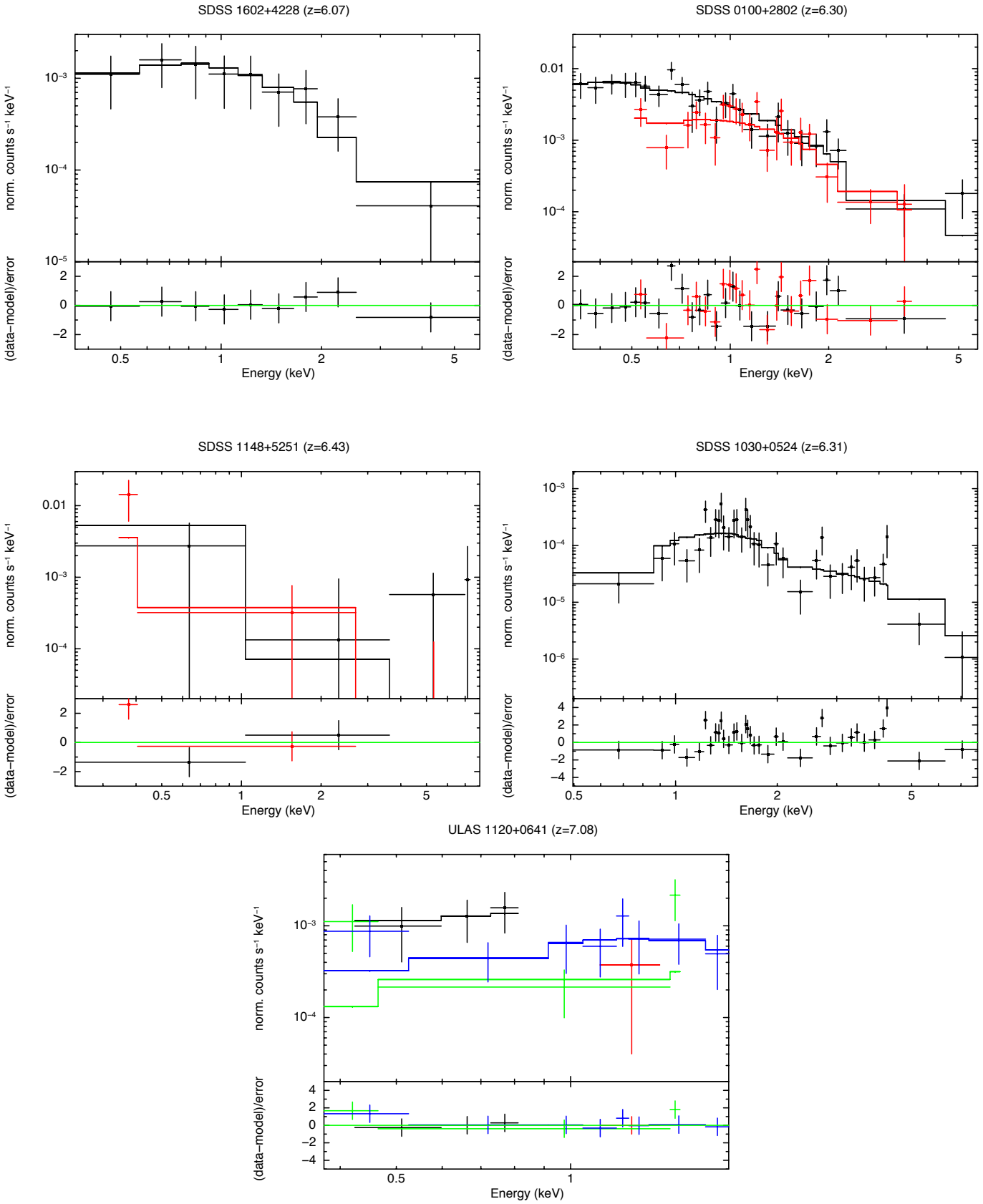

Fig. C.1. continued